



# High energy spinel-structured cathode stabilized by layered materials for advanced lithium-ion batteries

Jia Lu<sup>a</sup>, Ya-Lin Chang<sup>b</sup>, Bohang Song<sup>a</sup>, Hui Xia<sup>c</sup>, Jer-Ren Yang<sup>b</sup>, Kim Seng Lee<sup>a</sup>, Li Lu<sup>a,\*</sup>

<sup>a</sup> Department of Mechanical Engineering, National University of Singapore, Singapore 117575, Singapore

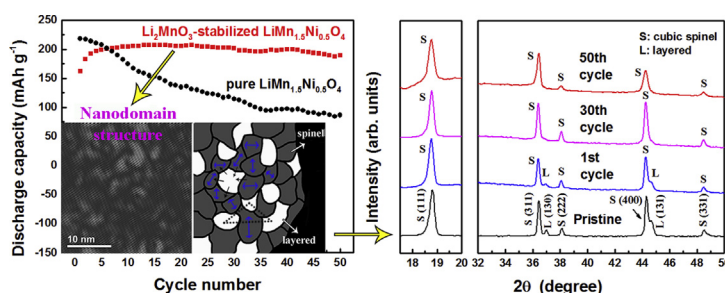
<sup>b</sup> Department of Materials Science and Engineering, National Taiwan University, Taipei 10617, Taiwan

<sup>c</sup> School of Materials Science and Engineering, Nanjing University of Science and Technology, Nanjing 210094, China

## HIGHLIGHTS

- $\text{Li}_2\text{MnO}_3$  nanodomains are embedded in  $\text{LiMn}_{1.5}\text{Ni}_{0.5}\text{O}_4$  matrix by co-precipitation method.
- $x\text{Li}_2\text{MnO}_3 \cdot (1-x)\text{LiMn}_{1.5}\text{Ni}_{0.5}\text{O}_4$  shows significantly improved cycling stability.
- Jahn–Teller distortion has been successfully suppressed with nanodomain structure.
- $0.3\text{Li}_2\text{MnO}_3 \cdot 0.7\text{LiMn}_{1.5}\text{Ni}_{0.5}\text{O}_4$  shows promise for high energy density Li-ion batteries.

## GRAPHICAL ABSTRACT



## ARTICLE INFO

### Article history:

Received 22 June 2014

Received in revised form

8 August 2014

Accepted 11 August 2014

Available online 20 August 2014

### Keywords:

Spinel structure

Stabilized cathodes

Cycle stability

High energy density

Lithium-ion batteries

## ABSTRACT

Due to well-known Jahn–Teller distortion in spinel  $\text{LiMn}_{1.5}\text{Ni}_{0.5}\text{O}_4$ , it can only be reversibly electrochemically cycled between 3 and 4.8 V with a limited reversible capacity of  $\sim 147 \text{ mAh g}^{-1}$ . This study intends to embed the layer-structured  $\text{Li}_2\text{MnO}_3$  nanodomains into  $\text{LiMn}_{1.5}\text{Ni}_{0.5}\text{O}_4$  spinel matrix so that the Jahn–Teller distortion can be suppressed even when the average Mn oxidation state is below +3.5. A series of  $x\text{Li}_2\text{MnO}_3 \cdot (1-x)\text{LiMn}_{1.5}\text{Ni}_{0.5}\text{O}_4$  where  $x = 0, 0.1, 0.2, 0.3, 0.4, 0.5$  and 1 are synthesized by co-precipitation method. The composites with intermediate values of  $x = 0.1, 0.2, 0.3, 0.4$  and 0.5 exhibit both spinel and layered structural domains in the particles and show greatly improved cycle stability than that of the pure spinel. Among them,  $0.3\text{Li}_2\text{MnO}_3 \cdot 0.7\text{LiMn}_{1.5}\text{Ni}_{0.5}\text{O}_4$  delivers the highest and almost constant capacity after a few conditional cycles and shows superior cycle stability. Ex-situ X-ray diffraction results indicate that no Jahn–Teller distortion occurs during the cycling of the  $0.3\text{Li}_2\text{MnO}_3 \cdot 0.7\text{LiMn}_{1.5}\text{Ni}_{0.5}\text{O}_4$  composite. Additionally,  $0.3\text{Li}_2\text{MnO}_3 \cdot 0.7\text{LiMn}_{1.5}\text{Ni}_{0.5}\text{O}_4$  possesses a high energy density of  $\sim 700 \text{ Wh kg}^{-1}$ , showing great promise for advanced high energy density lithium-ion batteries.

© 2014 Elsevier B.V. All rights reserved.

## 1. Introduction

Developing high energy and high power lithium-ion batteries for applications in electric vehicles (EVs) and hybrid-electric vehicles (HEVs) has attracted great attention [1,2]. However, current

cathode materials, such as  $\text{LiCoO}_2$ ,  $\text{LiMn}_2\text{O}_4$  and  $\text{LiFePO}_4$ , cannot meet the requirements of high energy density due to their limited specific capacities [3]. To achieve high energy and high power densities, it is highly important to develop new cathode materials with a large specific capacity and high operating voltage for the next generation of lithium-ion batteries. In recent years, spinel  $\text{LiMn}_{1.5}\text{Ni}_{0.5}\text{O}_4$  has attracted substantial interest as high energy and high power cathode material due to its high operating voltage of about 4.7 V, good cycle performance, and good rate capability as a

\* Corresponding author. Tel.: +65 65162236; fax: +65 67791459.

E-mail address: [luli@nus.edu.sg](mailto:luli@nus.edu.sg) (L. Lu).

result of three-dimensional  $\text{Li}^+$  ion diffusion channels [4–10].  $\text{LiMn}_{1.5}\text{Ni}_{0.5}\text{O}_4$  spinel is fundamentally different from  $\text{LiMn}_2\text{O}_4$  as all redox activity takes place on Ni with Mn theoretically remaining in 4+ state when cycled between 3 and 5 V, suppressing both Jahn–Teller distortion and Mn dissolution. In theory, the framework of  $\text{Mn}_{1.5}\text{Ni}_{0.5}\text{O}_4$  can accommodate two moles of  $\text{Li}^+$  with a specific capacity of about  $294 \text{ mAh g}^{-1}$  when Li ions are inserted into both 8a tetrahedral and 16c octahedral sites of the spinel lattice at the voltage of  $\sim 4.7 \text{ V}$  and  $\sim 2.8 \text{ V}$ , respectively [11–15]. However, for Jahn–Teller distortion at  $2.8 \text{ V}$  associated with a cubic to tetragonal phase transition, although the degree of distortion in  $\text{LiMn}_{1.5}\text{Ni}_{0.5}\text{O}_4$  ( $c/a = 1.07$ ) is smaller than that of  $\text{LiMn}_2\text{O}_4$  ( $c/a = 1.16$ ), there is still a big volume change of about 5% [16–19]. It is believed that the phase transition induced strain is too large for  $\text{LiMn}_{1.5}\text{Ni}_{0.5}\text{O}_4$  grains to maintain structural integrity, thus resulting in fast capacity fading upon cycling. By far,  $\text{LiMn}_{1.5}\text{Ni}_{0.5}\text{O}_4$  can only be reversibly charged and discharged between 3 and 5 V with limited capacity of  $147 \text{ mAh g}^{-1}$ , which hinders the use of  $\text{LiMn}_{1.5}\text{Ni}_{0.5}\text{O}_4$  for high energy applications. In order to practically use the theoretical capacity of  $294 \text{ mAh g}^{-1}$ , Jahn–Teller distortion in  $\text{LiMn}_{1.5}\text{Ni}_{0.5}\text{O}_4$  needs to be further suppressed to make this material can be reversibly charged and discharged between 2 and 5 V with 2  $\text{Li}^+$  extraction/reinsertion. To achieve this, cation and/or anion dopings in  $\text{LiMn}_{1.5}\text{Ni}_{0.5}\text{O}_4$  have been employed to suppress the Jahn–Teller distortion with improved cyclic performance between 2 and 5 V. Alcántara et al. [12] reported that Mg-doped  $\text{LiMn}_{1.5}\text{Ni}_{0.5}\text{O}_4$  exhibits a net improvement in capacity retention as Mg content increases when cycled in the 3 V region. Similarly, Lin et al. [15] reported that the Ti-doped  $\text{LiMn}_{1.5}\text{Ni}_{0.5}\text{O}_4$  exhibits improved capacity retention compared to the undoped  $\text{LiMn}_{1.5}\text{Ni}_{0.5}\text{O}_4$  in the wide voltage region of  $4.95\text{--}2.0 \text{ V}$ . However, it is worth noting that both Mg- and Ti-doping at either Ni or Mn site significantly decrease the reversible capacity of materials and cannot completely solve the problems associated with Jahn–Teller distortion. As a result, the obtained reversible capacity and cycle performance are still far from the requirements for practical applications.

Inspired by recent achievements in substitution of structural units rather than cations or anions, improved structural stability has been demonstrated by  $\text{Li}_2\text{MnO}_3$  stabilized layered  $\text{LiMO}_2$  (M refers to transition metals) in a wide voltage window between 2 and 5 V [20–23]. Since  $\text{Li}_2\text{MnO}_3$  is electrochemically inactive below 3 V [24], if the nano dimension  $\text{Li}_2\text{MnO}_3$  structural units can be embedded in the spinel structure, such nanostructure units may be able to help accommodate stress from the Jahn–Teller distortion, leading to improved structural stability of the spinel in a wide voltage window between 2 and 5 V. Moreover,  $\text{Li}_2\text{MnO}_3$  phase could be activated by extracting  $\text{Li}_2\text{O}$  from  $\text{Li}_2\text{MnO}_3$  to yield electrochemically active  $\text{MnO}_2$  at high voltage region and it will further contribute to the capacity of the composites. Despite the variation in crystallographic space group symmetry,  $R\bar{3}m$  (trigonal) for  $\text{LiMO}_2$  and  $Fd\bar{3}m$  (cubic) for  $\text{LiMn}_{1.5}\text{Ni}_{0.5}\text{O}_4$ , the structural compatibility in view of (001)<sub>monoclinic</sub> [20] and (111)<sub>cubic</sub> [25] lattice fringes [26] allows the integration of the  $\text{Li}_2\text{MnO}_3$  nanodomains in spinel  $\text{LiMn}_{1.5}\text{Ni}_{0.5}\text{O}_4$  with the success in the layered–layered composites. Unlike layered–layered composite structure in which the (001) and (003) lattice fringes of the  $\text{Li}_2\text{MnO}_3$  and  $\text{LiMO}_2$  are coincident in the HRTEM, it is more readily to differentiate two structurally compatible layered and spinel components with this technique [20].

In this work, a series of layered–spinel  $x\text{Li}_2\text{MnO}_3 \cdot (1-x)\text{LiMn}_{1.5}\text{Ni}_{0.5}\text{O}_4$  ( $x = 0.1, 0.2, 0.3, 0.4$  and  $0.5$ ) are prepared by co-precipitation method. We demonstrate that the layered  $\text{Li}_2\text{MnO}_3$  nanodomains are successfully embedded in the  $\text{LiMn}_{1.5}\text{Ni}_{0.5}\text{O}_4$  spinel particles so that  $\text{Li}_2\text{MnO}_3$  nanodomains are able to stabilize

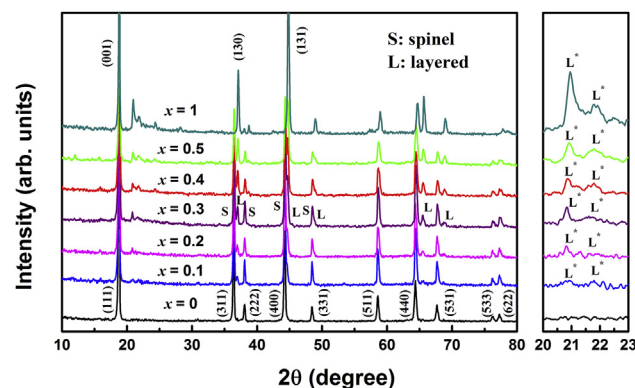


**Fig. 1.** Powder X-ray diffraction spectra of  $x\text{Li}_2\text{MnO}_3 \cdot (1-x)\text{LiMn}_{1.5}\text{Ni}_{0.5}\text{O}_4$  ( $x = 0, 0.1, 0.2, 0.3, 0.4, 0.5$  and  $1$ ). S and L refer, respectively, to the cubic spinel and layered phase;  $L^*$  refers the superstructure reflections arising from an ordering among  $\text{Li}^+$  and  $\text{Mn}^{4+}$  in the layered phase.

$\text{LiMn}_{1.5}\text{Ni}_{0.5}\text{O}_4$  providing a large reversible capacity of about  $200 \text{ mAh g}^{-1}$  where  $x = 0.3$  and excellent cycle stability in the wide voltage window between 2 and 4.8 V. The greatly improved cyclability of the spinel between 2 and 4.8 V can be attributed to the improved structural stability as a result of the dispersed  $\text{Li}_2\text{MnO}_3$  nanodomains in the spinel matrix, as ex-situ X-ray diffraction (XRD) confirms that no Jahn–Teller distortion takes place for this composite when discharged to 2 V.

## 2. Experimental

### 2.1. Materials synthesis

A series of  $x\text{Li}_2\text{MnO}_3 \cdot (1-x)\text{LiMn}_{1.5}\text{Ni}_{0.5}\text{O}_4$  ( $x = 0, 0.1, 0.2, 0.3, 0.4, 0.5$  and  $1$ ) composites were prepared via co-precipitation followed by calcination. In a typical synthesis, stoichiometric amounts of  $\text{NiSO}_4 \cdot 6\text{H}_2\text{O}$  and  $\text{MnSO}_4 \cdot \text{H}_2\text{O}$  were dissolved in distilled water and then added dropwise into a mixed aqueous solution of  $\text{Na}_2\text{CO}_3$  and  $\text{NH}_4\text{HCO}_3$  with continuous stirring. The obtained co-precipitated carbonate powders were then filtered, washed, and dried in an air oven at  $80^\circ\text{C}$ . Thereafter, the dried carbonate powders were mechanically mixed with required amounts of lithium carbonate. The mixtures were first heated at  $600^\circ\text{C}$  for 5 h and then calcined at  $900^\circ\text{C}$  for 10 h in air to obtain the final products. A 5 wt% excess lithium carbonate was used in the mixtures to compensate for lithium loss during the high temperature calcination process.

### 2.2. Materials characterization

The crystal structure of the as-prepared powders was characterized by X-ray diffraction (Shimadzu XRD-6000 Cu-K $\alpha$  radiation) in a  $2\theta$  range of  $10\text{--}80^\circ$  at a scan rate of  $2^\circ \text{ min}^{-1}$ . Morphology and microstructure of different samples were investigated by a field emission scanning electron microscopy (S-4300 Shimadzu, 15 kV) and a high resolution transmission electron microscope (FEI Tecnai G2 F20), respectively.

Electrochemical properties of the synthesized materials were evaluated using 2016-type coin cells assembled in an Ar-filled glove box. The electrodes were prepared by mixing 80 wt% active material, 10 wt% Super P carbon conducting additive, and 10 wt% polyvinylidene fluoride (PVDF) binder in a *N*-methyl-2-pyrrolidone (NMP) solution and stirred overnight for uniform mixing. Then the slurry was casted on circular aluminium foils and dried at  $120^\circ\text{C}$  for 24 h. Coin cells were assembled with the as-prepared cathode,

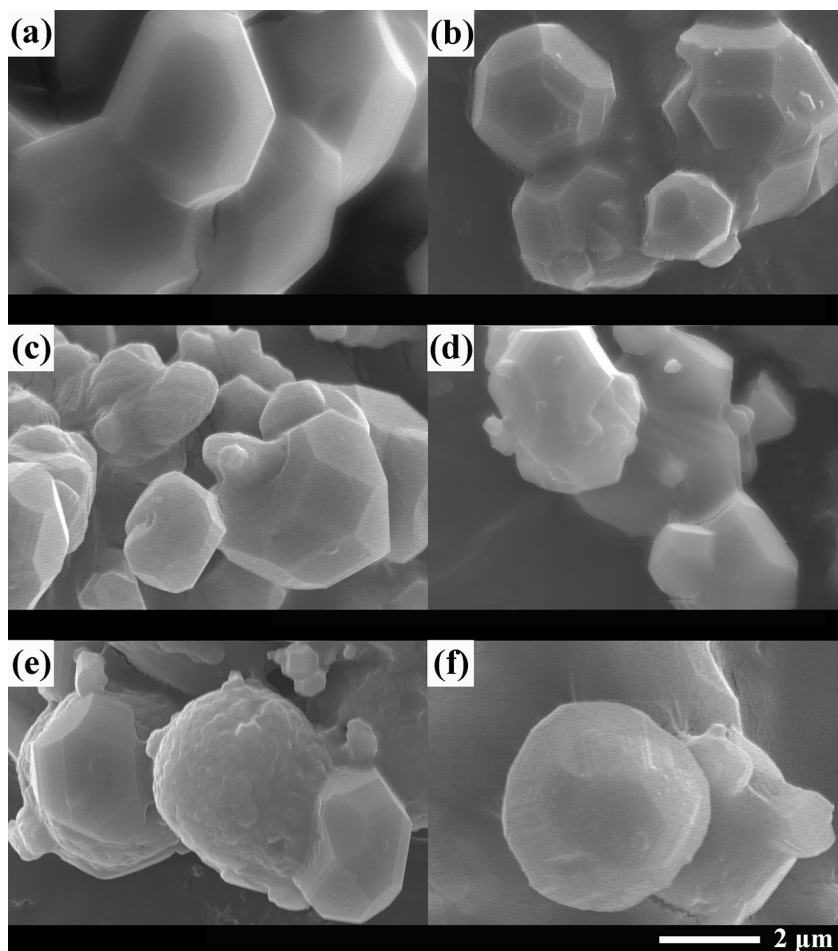


Fig. 2. SEM images of the  $x\text{Li}_2\text{MnO}_3 \cdot (1-x)\text{LiMn}_{1.5}\text{Ni}_{0.5}\text{O}_4$  (a)  $x = 0$  (b)  $x = 0.1$  (c)  $x = 0.2$  (d)  $x = 0.3$  (e)  $x = 0.4$  (f)  $x = 0.5$ .

lithium metal foil anode, two pieces of Celgard 2500 as the separators and 1 M  $\text{LiPF}_6$  in ethylene carbonate (EC)/diethyl carbonate (DEC) (1:1, v/v) as the electrolyte. Galvanostatic charge/discharge measurements were carried out at current densities from  $20 \text{ mA g}^{-1}$  ( $\sim 0.1 \text{ mA cm}^{-2}$ ) to  $2000 \text{ mA g}^{-1}$  between 2.0 and 4.8 V at room temperature using a Neware battery test station. For the ex-situ XRD analysis, coin cells at various discharge states were disassembled in the Ar-filled glove box. The obtained electrodes were gently washed with dimethyl carbonate (DMC) and dried at room temperature for characterization. Electrochemical impedance spectroscopy (EIS) measurements were performed on a Solartron 1260 + 1287 System at a frequency range from 100 kHz to 0.01 Hz with an AC voltage amplitude of 5 mV.

### 3. Results and discussion

#### 3.1. Structural analysis

The XRD spectra of  $x\text{Li}_2\text{MnO}_3 \cdot (1-x)\text{LiMn}_{1.5}\text{Ni}_{0.5}\text{O}_4$  with  $x = 0, 0.1, 0.2, 0.3, 0.4, 0.5$  and 1 calcined at  $900^\circ\text{C}$  are shown in Fig. 1. When  $x = 0$  and  $x = 1$ , the two XRD patterns can be indexed as a disordered cubic spinel phase with symmetry and a monoclinic phase with symmetry, respectively. For the intermediate compositions of  $x = 0.1, 0.2, 0.3, 0.4$  and  $0.5$ , XRD spectra show reflection peaks corresponding to both layered and spinel phases, indicating the coexistence of these two phases in the products. The several weak peaks located in the  $2\theta$  range of  $20\text{--}23^\circ$ , shown in the right enlarged section, are consistent with the  $\text{LiMn}_6$  super-ordering in

$\text{Li}_2\text{MnO}_3$  monoclinic phase [20]. As expected, the intensities of these weak peaks increase as  $x$  increases, indicating a larger content of layered phase is formed in the composite.

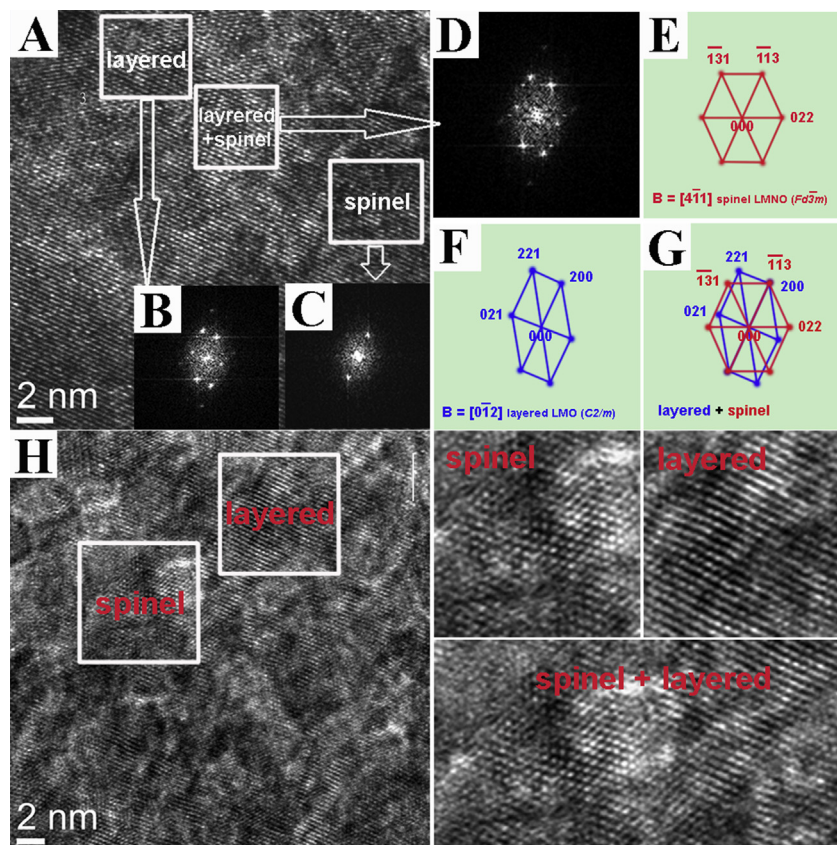
#### 3.2. Particle morphology

Fig. 2 shows the SEM images of the  $x\text{Li}_2\text{MnO}_3 \cdot (1-x)\text{LiMn}_{1.5}\text{Ni}_{0.5}\text{O}_4$  ( $x = 0, 0.1, 0.2, 0.3, 0.4$  and  $0.5$ ) composites. It can be seen that the average particle size is about  $2 \mu\text{m}$  and the overall particle morphologies are little different from each other according to the compositions. The pure spinel oxide as shown in Fig. 2a is composed of well-formed polyhedrons while the samples with high amount of  $\text{Li}_2\text{MnO}_3$  are composed of particles without well-defined edges, indicating that the morphology of particles is affected by the amount of layered  $\text{Li}_2\text{MnO}_3$ .

#### 3.3. Microstructure observation

Fig. 3 shows HRTEM images of  $0.3\text{Li}_2\text{MnO}_3 \cdot 0.7\text{LiMn}_{1.5}\text{Ni}_{0.5}\text{O}_4$ . In view of the bulk area as shown in HRTEM image A, the layered, spinel as well as the layered-spinel intermediate zones could be easily identified and all within different nanodomains in one particle. Moreover, the Fast Fourier Transformation (FFT) images with corresponding indexing results for these areas are shown in panel B, C and D along with F, E and G, respectively, showing the spatial relationship among these nanodomains. The intermediate zones contain both integrated layered and spinel orderings. Fig. 3H shows the remarkable topotactic coexistence of layered and spinel regions





**Fig. 3.** TEM identification of  $x = 0.3$  particles. A. HRTEM image in bulk region shows layered, spinel and layered-spinel intermediate nano-domain structures. The fast Fourier transformation (FFT) to Panel A is shown in Panel B, C and D which are indexed as in Panel F, E and G, respectively. H. HRTEM image and corresponding magnifications of spinel, layered and layered-spinel intermediate zones.

in which the close-packed planes of the layered  $\text{Li}_2\text{MnO}_3$  and spinel component are coherent along  $\text{Li}_2\text{MnO}_3$  [200] and spinel  $[\bar{1}\bar{1}3]$  direction. The HRTEM results clearly indicate that the layered nano-domains were successfully embedded in the spinel structure.

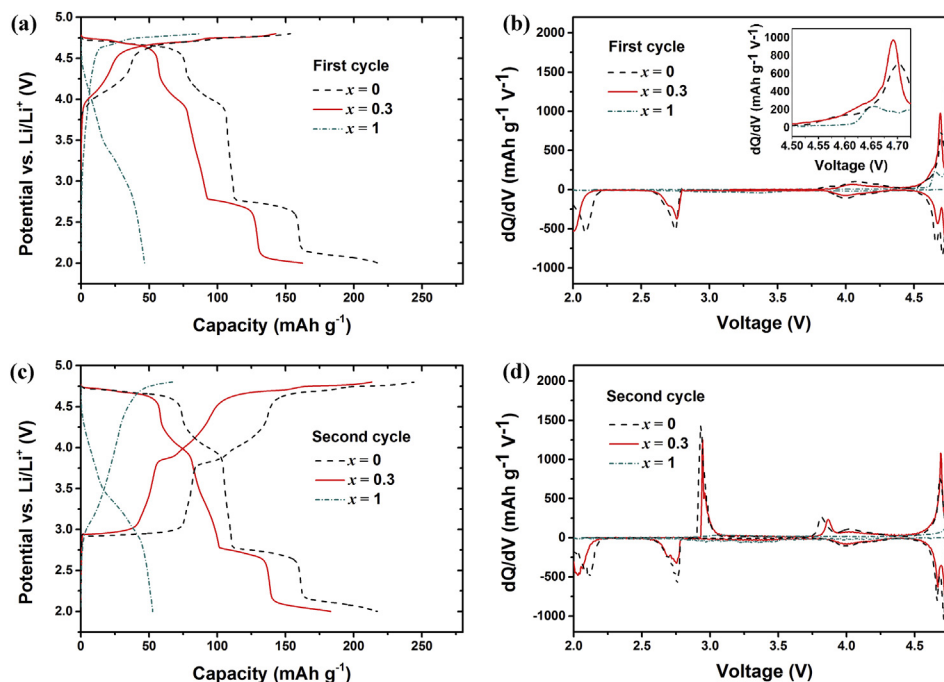
#### 3.4. First and second cycle charge–discharge profiles

Fig. 4a shows the first cycle charge–discharge profiles of the pure  $\text{Li}_2\text{MnO}_3$ ,  $\text{LiMn}_{1.5}\text{Ni}_{0.5}\text{O}_4$  and  $0.3\text{Li}_2\text{MnO}_3 \cdot 0.7\text{LiMn}_{1.5}\text{Ni}_{0.5}\text{O}_4$  at a current density of  $20 \text{ mA g}^{-1}$  between 2.0 and 4.8 V. For  $x = 0$ , the charge curve of  $\text{LiMn}_{1.5}\text{Ni}_{0.5}\text{O}_4$  exhibits three voltage plateaus whereas five distinctive discharge plateaus are observed, representing a typical voltage response of a pure spinel electrode [14]. During charge, the two voltage plateaus at about 4.7 V are associated with the oxidation of  $\text{Ni}^{2+}$  to  $\text{Ni}^{3+}$  and  $\text{Ni}^{3+}$  to  $\text{Ni}^{4+}$ . Upon discharge, first two plateaus at about 4.7 V correspond to the reduction of, respectively,  $\text{Ni}^{4+}$  to  $\text{Ni}^{3+}$  and  $\text{Ni}^{3+}$  to  $\text{Ni}^{2+}$  with  $\text{Li}^+$  ion insertion into the tetrahedral sites of the cubic spinel structure. The plateaus at  $\sim 4.0 \text{ V}$  for both charge and discharge originate from the redox reaction of  $\text{Mn}^{3+}/\text{Mn}^{4+}$ , which is caused by the deficit of small amount oxygen in the pristine sample. Further discharging the sample below 3 V results in another two plateaus at about 2.8 and 2.1 V, respectively. The two plateaus can be attributed to the reduction of  $\text{Mn}^{4+}$  to  $\text{Mn}^{3+}$  involving Li ion insertion into 16c octahedral sites of the spinel structure, which is associated with a cubic to tetragonal phase transition. For  $x = 1$ , the charge–discharge profiles are consistent with the electrochemical response of pure layered  $\text{Li}_2\text{MnO}_3$  electrode. During the initial charge, a voltage plateau-like region at  $\sim 4.6 \text{ V}$  is originated from the irreversible removal of  $\text{Li}_2\text{O}$  from  $\text{Li}_2\text{MnO}_3$  to form  $\text{MnO}_2$ . During

the discharge, the steadily decreasing voltage profile is consistent with the insertion of Li ion into  $\text{MnO}_2$  structure [27,28]. For the composite with intermediate composition  $0.3\text{Li}_2\text{MnO}_3 \cdot 0.7\text{LiMn}_{1.5}\text{Ni}_{0.5}\text{O}_4$ , the initial charge and discharge voltage profile shows both the spinel- and layered-like feature. Upon discharge, the sloping profile between 3.9 and 2.8 V is a signature of the presence of the layered component while the voltage plateaus above 4.5 V and below 2.8 V are associated with the spinel component. Moreover, this trend is also supported by the  $dQ/dV$  analysis in Fig. 4. The small peak corresponding to the activation of  $\text{Li}_2\text{MnO}_3$  in the pure layered and the  $0.3\text{Li}_2\text{MnO}_3 \cdot 0.7\text{LiMn}_{1.5}\text{Ni}_{0.5}\text{O}_4$  composite are easily observed in the enlarged section of the  $dQ/dV$  plots compared with pure spinel composite (Fig. 4b). For the second cycle, two new voltage plateaus at about 2.9 V and 3.82 V emerge in the charge curves for both the pure spinel and the  $0.3\text{Li}_2\text{MnO}_3 \cdot 0.7\text{LiMn}_{1.5}\text{Ni}_{0.5}\text{O}_4$  composite, corresponding to the tetragonal to cubic phase transition involving the oxidation of  $\text{Mn}^{3+}$  to  $\text{Mn}^{4+}$ .

#### 3.5. Compositional phase diagram

A proposed electrochemical reaction mechanism of the  $x\text{Li}_2\text{MnO}_3 \cdot (1-x)\text{LiMn}_{1.5}\text{Ni}_{0.5}\text{O}_4$  electrode is illustrated in the compositional phase diagram as shown in Fig. 5. The chemical composition of  $0.3\text{Li}_2\text{MnO}_3 \cdot 0.7\text{LiMn}_{1.5}\text{Ni}_{0.5}\text{O}_4$  is located at the point of  $x = 0.3$  in the  $\text{Li}_2\text{MnO}_3$ – $\text{LiMn}_{1.5}\text{Ni}_{0.5}\text{O}_4$  tie line. During the initial charge of the  $\text{Li}/0.3\text{Li}_2\text{MnO}_3 \cdot 0.7\text{LiMn}_{1.5}\text{Ni}_{0.5}\text{O}_4$  cell to about 4.6 V,  $\text{Li}^+$  ions are first extracted from  $\text{Li}_2\text{MnO}_3$  before they are extracted from  $\text{LiMn}_{1.5}\text{Ni}_{0.5}\text{O}_4$  as indicated by the solid line in the compositional phase diagram. In this case,  $\text{MnO}_2$  is formed with the simultaneous release of oxygen. When the cell voltage is raised to higher value,  $\text{Li}^+$



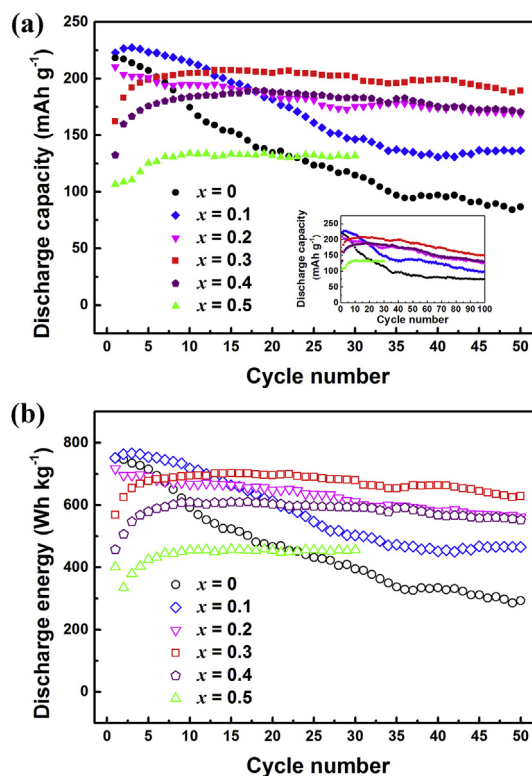
**Fig. 4.** (a) First cycle and (c) second cycle charge–discharge profiles and (b) first cycle and (d) second cycle differential capacity ( $dQ/dV$ ) plots of three composites  $x\text{Li}_2\text{MnO}_3 \cdot (1-x)\text{LiMn}_{1.5}\text{Ni}_{0.5}\text{O}_4$  ( $x = 0, 0.3, 1$ ) when cycled between 2.0 and 4.8 V at  $20 \text{ mA g}^{-1}$ .

ions are further extracted from the  $\text{LiMn}_{1.5}\text{Ni}_{0.5}\text{O}_4$  component in the composite with formation of  $\text{Mn}_{1.5}\text{Ni}_{0.5}\text{O}_4$  until the solid line reaches the  $\text{Li}_2\text{MnO}_3\text{--Mn}_2\text{O}_4$  ( $\text{MnO}_2 \cdot \text{Mn}_{1.5}\text{Ni}_{0.5}\text{O}_4$ ) tie line. Finally, the composition of the electrode becomes  $(x-\delta)\text{Li}_2\text{MnO}_3 \cdot \delta\text{MnO}_2 \cdot (1-x)\text{Mn}_{1.5}\text{Ni}_{0.5}\text{O}_4$  at the end of the charge process. On the following discharge process, the  $\text{Li}^+$  ions are firstly inserted into the spinel component and then into the  $\text{MnO}_2$  component until the final composition  $(x-\delta)\text{Li}_2\text{MnO}_3 \cdot \delta\text{LiMnO}_2 \cdot (1-x)\text{Li}_2\text{Mn}_{1.5}\text{Ni}_{0.5}\text{O}_4$  is reached as indicated by the dash line in the compositional phase diagram. After that, the compositional changes of  $x\text{Li}_2\text{MnO}_3 \cdot (1-x)\text{LiMn}_{1.5}\text{Ni}_{0.5}\text{O}_4$  could be expected to follow the  $(x-\delta)\text{Li}_2\text{MnO}_3 \cdot \delta\text{MnO}_2 \cdot (1-x)\text{Mn}_{1.5}\text{Ni}_{0.5}\text{O}_4\text{--}(x-\delta)\text{Li}_2\text{MnO}_3 \cdot \delta\text{LiMnO}_2 \cdot (1-x)\text{Li}_2\text{Mn}_{1.5}\text{Ni}_{0.5}\text{O}_4$  tie-line in Fig. 5.

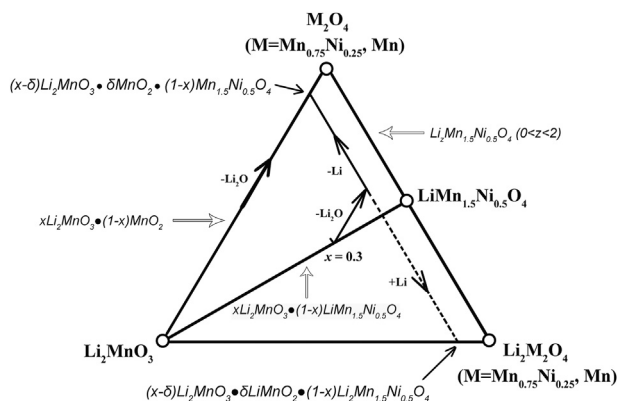
### 3.6. Cycle performance

Fig. 6a shows the discharge capacity versus cycle number for the first 50 cycles of the various lithium cells when cycled between 2 and 4.8 V. The data clearly demonstrate that the capacity of the

$x\text{Li}_2\text{MnO}_3 \cdot (1-x)\text{LiMn}_{1.5}\text{Ni}_{0.5}\text{O}_4$  electrode in the first cycle decreases with increase in the amount of  $x$ , which is attributed to the increased amount of electrochemically inactive  $\text{Li}_2\text{MnO}_3$  phase in the composite. As can be seen, the spinel electrode  $\text{LiMn}_{1.5}\text{Ni}_{0.5}\text{O}_4$  ( $x = 0$ ) delivers the highest initial discharge capacity of



**Fig. 6.** Cycle performance of the  $x\text{Li}_2\text{MnO}_3 \cdot (1-x)\text{LiMn}_{1.5}\text{Ni}_{0.5}\text{O}_4$  electrodes ( $x = 0, 0.1, 0.2, 0.3, 0.4$  and  $0.5$ ) when cycled between 2 and 4.8 V at  $20 \text{ mA g}^{-1}$ : (a) discharge capacity and (b) discharge energy density.



**Fig. 5.** Compositional phase diagram showing the electrochemical reaction pathways for a  $x\text{Li}_2\text{MnO}_3 \cdot (1-x)\text{LiMn}_{1.5}\text{Ni}_{0.5}\text{O}_4$  electrode.

$\sim 220 \text{ mAh g}^{-1}$ . However, the discharge capacity for the pure spinel decreases sharply over successive cycles. It is clear that the incorporation of  $\text{Li}_2\text{MnO}_3$  nanodomains in the spinel matrix could greatly improve the cycle stability as all composites with various  $x$  values exhibit significantly improved capacity retention. There is a tendency that the capacity retention of the composite can be further improved as the content of  $\text{Li}_2\text{MnO}_3$  component increases. However, excessive inactive  $\text{Li}_2\text{MnO}_3$  embedded in the spinel structure will decrease the total specific capacity, such as the samples with  $x = 0.4$  and  $x = 0.5$ . Among various compositions, the  $x = 0.3$  electrode is the most promising one because it shows a good combination of high capacity and good cycle stability, even after 100 cycles as shown in Fig. 6a. Similarly, the same trend is also found in the discharge energy density variation as a function of cycle number as shown in Fig. 6b.

In order to further investigate the cycle stabilities of both the spinel and layered components in the  $x = 0.3$  composite, comparisons of the cyclability at different potential windows between the pure spinel and  $x = 0.3$  composite are shown in Fig. 7. As discussed, the capacities generated above 4.5 V and below 2.8 V are contributed by the spinel component. Fig. 7 reveals that the cycle stability of the spinel component in the composite has been significantly improved compared to the pure spinel. However, it is worth noting that the layered component is gradually activated during the extend cycling and contributes to total capacity. Since the reversible capacity of the  $\text{Li}_2\text{MnO}_3$  component in this sample is  $50 \text{ mAh g}^{-1}$  (the mass of  $0.3\text{Li}_2\text{MnO}_3 \cdot 0.7\text{LiMn}_{1.5}\text{Ni}_{0.5}\text{O}_4$  is used in the calculation), the data in Fig. 7c clearly demonstrate that nearly all the  $\text{Li}_2\text{MnO}_3$  component in  $0.3\text{Li}_2\text{MnO}_3 \cdot 0.7\text{LiMn}_{1.5}\text{Ni}_{0.5}\text{O}_4$  composite has been activated after 15 cycles. Therefore, the embedded  $\text{Li}_2\text{MnO}_3$  nanodomain in the spinel not only improve the cycle stability of spinel component but also contribute to the total reversible capacity for the composite.

Fig. 8 shows ex-situ XRD to understand structural changes of the two types of materials after discharged to 2 V. Fig. 8a reveals the XRD spectra of the pure spinel before and after the first cycle

charge/discharge at the current density of  $20 \text{ mA g}^{-1}$  between 4.8 and 2 V. It is noted that predominant diffraction from tetragonal phase belonging to the space group clearly appeared after the first discharge, whereas no structural changes are observed from  $0.3\text{Li}_2\text{MnO}_3 \cdot 0.7\text{LiMn}_{1.5}\text{Ni}_{0.5}\text{O}_4$  sample, even after 50th cycle (Fig. 8b), indicating that the Jahn–Teller distortion is completely suppressed due to the presence of layered nanodomain in the spinel. This conclusion is also consistent with the good cycle performance for the  $x = 0.3$  sample. However, it is worth noting that after the 30th cycle, the apparent reflections corresponding to the layered phase at  $37^\circ$  and  $44.8^\circ$  have almost completely disappeared. The reason for this phenomenon will be discussed in the following sections.

### 3.7. Mechanism for improved cycle performance

It is well known that fast capacity fade of  $\text{LiMn}_2\text{O}_4$  spinel takes place when average oxidation state of Mn ion is below 3.5. When the average oxidation state of Mn is below 3.5, the electrode will experience a slow surface dissolution into the electrolyte according to the disproportionation reaction:  $2\text{Mn}^{3+} \rightarrow \text{Mn}^{4+} + \text{Mn}^{2+}$ . At the same time, high  $\text{Mn}^{3+}$  concentration in the electrode will also induce a crystallographic Jahn–Teller distortion involving a large volume change [29]. Therefore, the possible reasons for the significant improvement in the cycle stability of  $x\text{Li}_2\text{MnO}_3 \cdot (1-x)\text{LiMn}_{1.5}\text{Ni}_{0.5}\text{O}_4$  composites can be ascribed into three aspects, namely suppression of surface manganese dissolution, elimination of Jahn–Teller distortion, and formation of spinel nanodomains.

Table 1 tabulates the average oxidation states of Mn ions in the fully discharged state of 2 V assuming no  $\text{Li}_2\text{MnO}_3$  has been activated. As can be seen, the average oxidation state of the Mn ions is as low as 3.33 when  $x = 0$ . Oxidation state increases with  $x$  value. When  $x = 0.4$  and  $0.5$ , it is larger than 3.5 while when  $x = 0.3$ , it is very close to 3.5. In general, greater cycle stability can be achieved in spinel oxides if the average oxidation state of the Mn ions is maintained above 3.5 throughout charge and discharge [30–32].

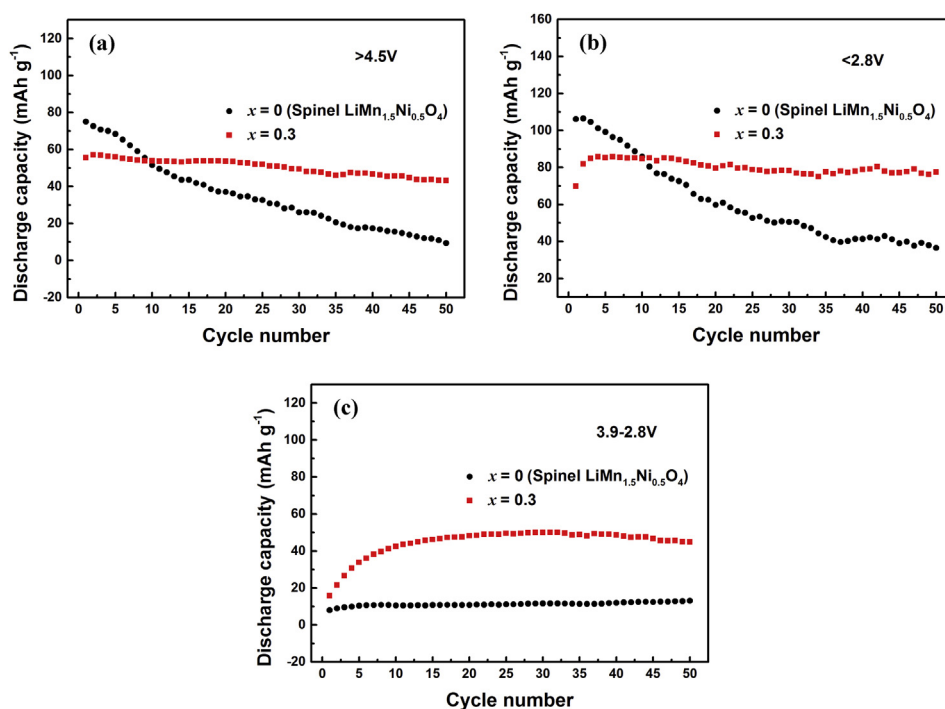
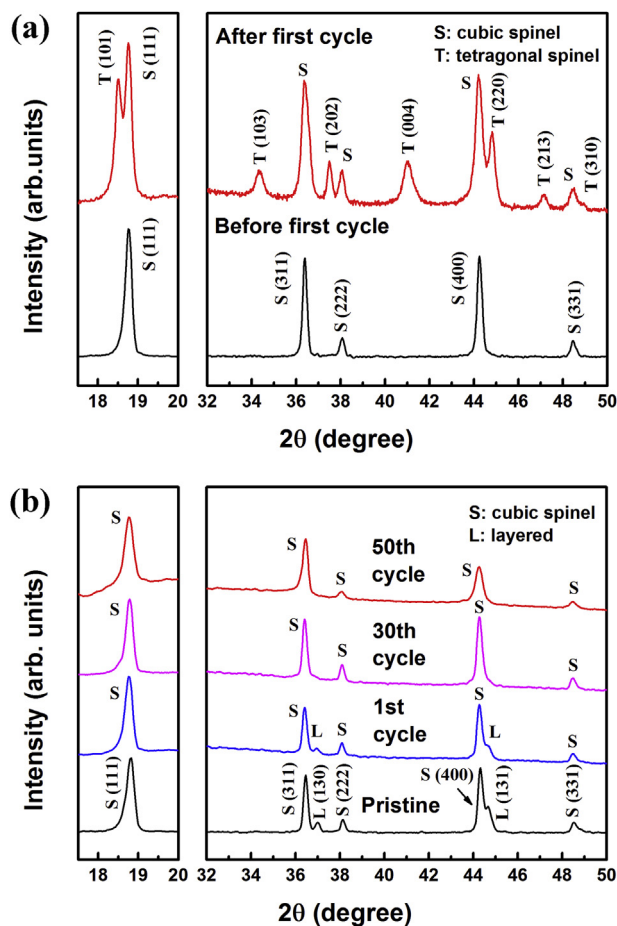


Fig. 7. Cycle performance of the  $x = 0.3$  sample in the  $x\text{Li}_2\text{MnO}_3 \cdot (1-x)\text{LiMn}_{1.5}\text{Ni}_{0.5}\text{O}_4$  system at different potential windows (a) 4.8–4.5 V (b) 2.8–2.0 V (c) 3.9–2.8 V in comparison with pure spinel  $\text{LiMn}_{1.5}\text{Ni}_{0.5}\text{O}_4$ .





**Fig. 8.** XRD data of (a) the  $x = 0$  and (b) the  $x = 0.3$  sample in the  $x\text{Li}_2\text{MnO}_3 \cdot (1 - x)\text{LiMn}_{1.5}\text{Ni}_{0.5}\text{O}_4$  system (before and after cycling). S, T and L refer, respectively, to the cubic spinel, tetragonal spinel and layered phase.

Therefore, one possible reason for the highly improved cycle stability of  $0.3\text{Li}_2\text{MnO}_3 \cdot 0.7\text{LiMn}_{1.5}\text{Ni}_{0.5}\text{O}_4$  in the present study can be attributed to high average valence of Mn ions, which can suppress the surface manganese dissolution.

Fig. 9 shows the HRTEM image and FFT patterns of different areas for a cycled pure spinel particle. In the cycled sample, distorted lattice/amorphous phases are easily observed in between the spinel domains as labelled by the red area (I) in Fig. 9A, which should be due to the strains associated with Jahn–Teller distortion. Moreover, the visualization of lattice distortion can also be directly seen from the elongation of the diffraction spots in panel B [33]. Such lattice distortion associated with large strain will lead to particle pulverization after repeated cycles. As shown in the inset of

Fig. 10A, the as-prepared  $\text{LiMn}_{1.5}\text{Ni}_{0.5}\text{O}_4$  particles display a dense structure without any cracks in the compact grains. After cycling test, however, the original large particles are pulverized into small ones and cracks are clearly observed in the large particles. The TEM results indicate the Jahn–Teller distortion induced strain is too large for the grains to maintain structural integrity and grains tend to break up, which could result in loss of electrical contact between electrode and current collector and thus fast capacity fade. On the contrary, no crack could be found in the  $0.3\text{Li}_2\text{MnO}_3 \cdot 0.7\text{LiMn}_{1.5}\text{Ni}_{0.5}\text{O}_4$  sample as shown in Fig. 10B. Consequently, it can be further concluded that the excellent cycling performance is obtained may be due to the good structural stability of the  $\text{Li}_2\text{MnO}_3$  integrated spinel material [34].

In the case when two phases coexist, growth of each phase will be constrained by another phase due to coherency and/or semi-coherency. The Fourier-filtered TEM image in Fig. 11A further highlights the nano-domain structure of average dimensions 30–60 Å. With such nanodomain structure (illustrated in Fig. 11B), the distortion of  $\text{LiMn}_{1.5}\text{Ni}_{0.5}\text{O}_4$  domains during charge and discharge has been constrained. Specifically, since the layered component is relatively stable during cycling, it could form a stable framework around the spinel component and suppress the Jahn–Teller distortion in  $\text{LiMn}_{1.5}\text{Ni}_{0.5}\text{O}_4$  component. Meanwhile part of the overall lithium concentration may be accommodated at interface sites, leaving the bulk of the cubic spinel regions lithium deficient [35]. Ex-situ XRD results provide a strong evidence for this speculation. Furthermore, even if the Jahn–Teller distortion still takes place during the cycling, the nanodomain structure can also help to accommodate large strain associated with the phase transition by slippage at the domain wall boundaries [36,37]. On the other hand, as reported [38], when the spinel domains become very small, the deformation of each domain in particles due to the formation of the tetragonal phase proceeds in random direction, resulting in less anisotropic deformation of the particles. In this case, the possibility of particle pulverization is greatly reduced.

Finally, the cycle stability of the layered  $\text{Li}_2\text{MnO}_3$  component is also concerned in this study. Fig. 8b shows the intensities of the reflections corresponding to the layered phase have almost disappeared in the XRD pattern after 30th cycles charge/discharge. As can be seen in Fig. 12, the discharge voltage profile between 3.9 and 2.8 V corresponding to the layered component, as discussed, shift towards the lower voltage profile (represented by arrow mark). This phenomenon has already been observed in the layered–layered system like  $x\text{Li}_2\text{MnO}_3 \cdot (1 - x)\text{LiMn}_{0.5}\text{Ni}_{0.5}\text{O}_2$  [39], which is related to the transition from a layered structure to a spinel-like structure. Other than regular spinel, most of the capacity obtained from this kind of material can continue to be delivered. With generation of such nanostructured spinel-like phase within the layered  $\text{Li}_2\text{MnO}_3$  domains, it will continue to serve the same purpose as its parent phase as reported by Armstrong et al. [36]. Therefore, although a layered to spinel phase transition takes place in the  $\text{Li}_2\text{MnO}_3$  component, excellent structural stability for the  $x\text{Li}_2\text{MnO}_3 \cdot (1 - x)\text{LiMn}_{1.5}\text{Ni}_{0.5}\text{O}_4$  composite is remained with cycling.

### 3.8. Rate capability

In order to further evaluate the  $\text{Li}_2\text{MnO}_3$  layered phase on the rate capability of the  $x\text{Li}_2\text{MnO}_3 \cdot (1 - x)\text{LiMn}_{1.5}\text{Ni}_{0.5}\text{O}_4$  composites, the cells were cycled in the voltage range of 2.0–4.8 V with the increasing current densities from  $20 \text{ mA g}^{-1}$  to  $2000 \text{ mA g}^{-1}$ . The rate capability of  $x\text{Li}_2\text{MnO}_3 \cdot (1 - x)\text{LiMn}_{1.5}\text{Ni}_{0.5}\text{O}_4$  is displayed in Fig. 13a. The cells are charged and discharged at the same rate. It clearly reveals when the applied current density increases, all the samples show gradual decreases of the discharge capacity, which is

**Table 1**

Average oxidation states of manganese and nickel ions in the discharged  $x\text{Li}_2\text{MnO}_3 \cdot (1 - x)\text{LiMn}_{1.5}\text{Ni}_{0.5}\text{O}_4$  composites.

Compound	$x$	Mn oxidation state	Ni oxidation state
$x\text{Li}_2\text{MnO}_3 \cdot (1 - x)\text{LiMn}_{1.5}\text{Ni}_{0.5}\text{O}_4$	0	3.33+	2+
	0.1	3.38+	2+
	0.2	3.43+	2+
	0.3	3.48+	2+
	0.4	3.54+	2+
	0.5	3.60+	2+
	1	4+	–

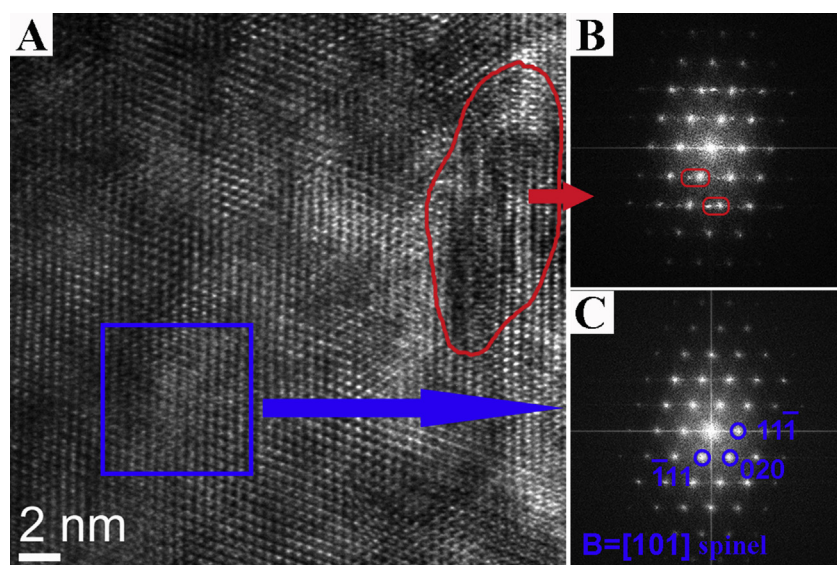


**Fig. 9.** Illustration of lattice distortion in pure spinel oxide A. HRTEM image in bulk region for a cycled spinel particle: cubic spinel is labelled with blue square while area circled by red shows lattice distortion. The fast fourier transformation (FFT) to Panel A is shown in Panel B and C: the elongation of the diffraction spots in Panel B indicates distortion of the lattices. (For interpretation of the references to colour in this figure legend, the reader is referred to the web version of this article.)

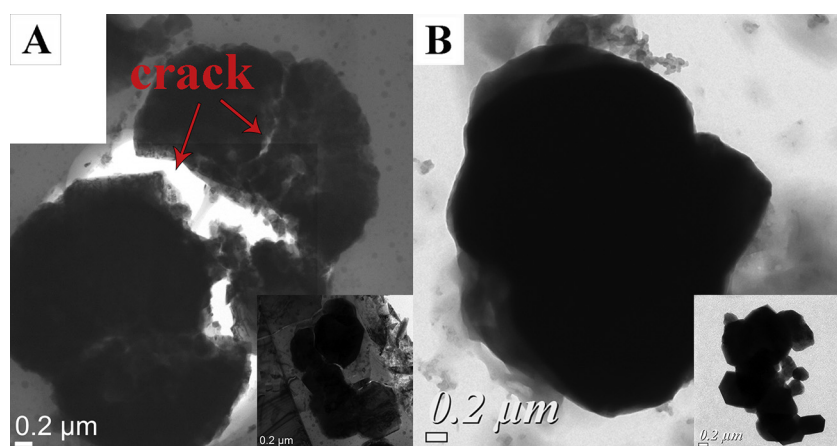


**Fig. 10.** HRTEM images of A. pure spinel and B.  $0.3\text{Li}_2\text{MnO}_3 \cdot 0.7\text{LiMn}_{1.5}\text{Ni}_{0.5}\text{O}_4$  particles before cycling (shown in the inset) and after the 30th cycle.

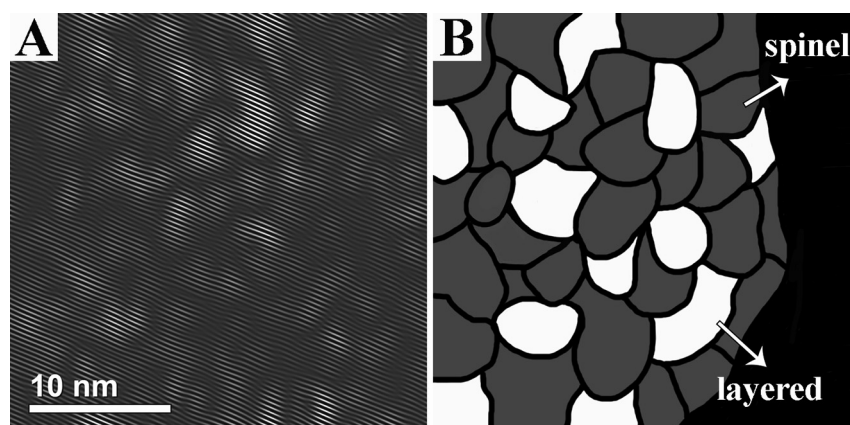


**Fig. 11.** A. Fourier-filtered TEM image of nanostructured  $0.3\text{Li}_2\text{MnO}_3 \cdot 0.7\text{LiMn}_{1.5}\text{Ni}_{0.5}\text{O}_4$  composite, B. A schematic representation of the nanodomain structure of  $0.3\text{Li}_2\text{MnO}_3 \cdot 0.7\text{LiMn}_{1.5}\text{Ni}_{0.5}\text{O}_4$  composite showing cubic spinel and layered nanodomains.



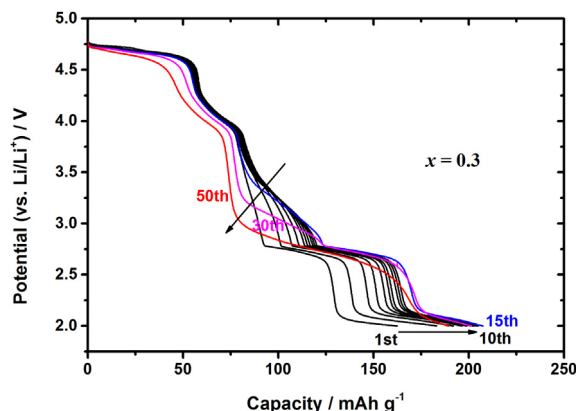


Fig. 12. Discharge profiles of the  $x = 0.3$  sample at the different cycles when cycled between 4.8 and 2 V at 20 mA  $g^{-1}$ .

attributed to the increasing polarization of the electrodes at high current densities [40]. Moreover, at the end of the test five additional cycles at 20 mA  $g^{-1}$  prove that the initial high capacity of the first five cycles is retained after cycling at high current densities in all tests. Due to difference in the initial capacity, the rate performance is therefore normalized by the discharge capacity at 0.1 C where 1 C = 20 mA  $g^{-1}$  and shown in Fig. 13b. It can be seen from Fig. 13b that the capacity retention of  $xLi_2MnO_3 \cdot (1-x)LiMn_{1.5}Ni_{0.5}O_4$  decreases with the increase of  $x$  value at every discharge rate.

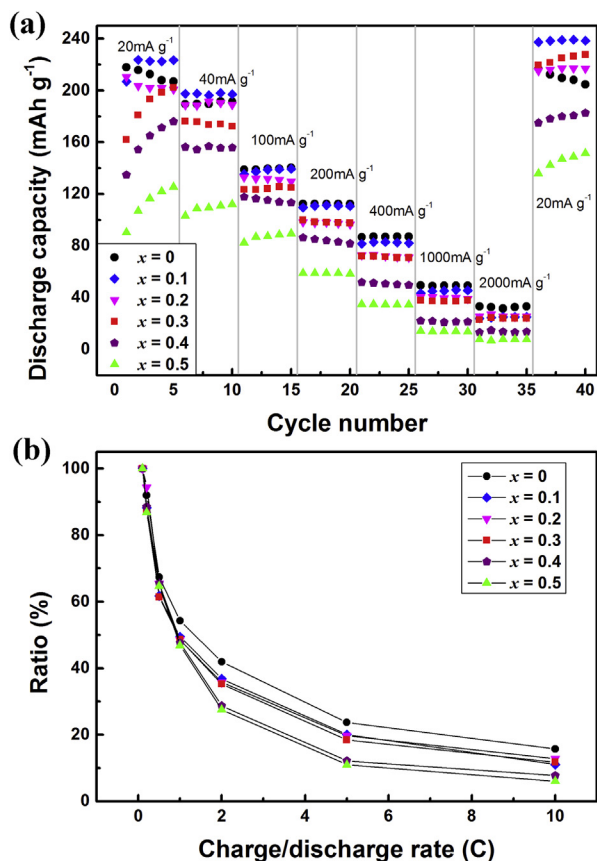


Fig. 13. (a) Rate capability of  $xLi_2MnO_3 \cdot (1-x)LiMn_{1.5}Ni_{0.5}O_4$  electrodes, the cells are charged and discharged at the same current densities (b) rate capabilities retain ratio (vs 0.1 C) of the  $xLi_2MnO_3 \cdot (1-x)LiMn_{1.5}Ni_{0.5}O_4$ .

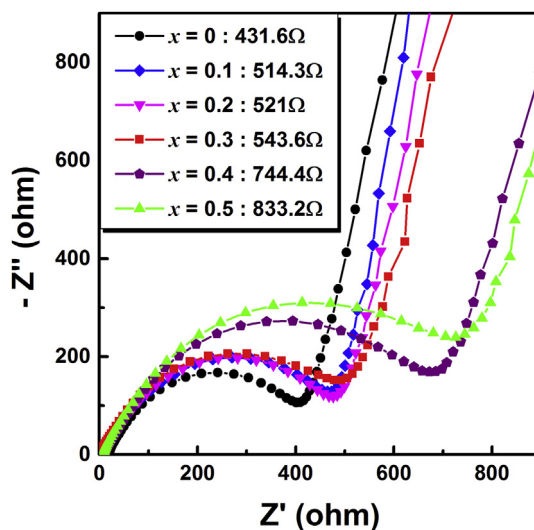


Fig. 14. Nyquist plots and equivalent circuit of  $xLi_2MnO_3 \cdot (1-x)LiMn_{1.5}Ni_{0.5}O_4$  ( $x = 0, 0.1, 0.2, 0.3, 0.4$  and  $0.5$ ).

Electrochemical impedance spectroscopy (EIS) has been performed to further understand the origins of the differences in the electrochemical performance of different electrodes. Fig. 14 reveals EIS plot of the electrodes before charge/discharge. As can be seen, the shapes of the Nyquist plots that are composed of a small interrupt, a semicircle and a quasi-straight line are all similar. Among them, the small interrupt that corresponds to the solution impedance ( $R_0$ ), is almost the same for all the electrodes. The semicircle is assigned to the impedance of  $Li^+$  diffusion in the surface layer, which is related to the charge-transfer reaction, the so-called charge transfer reaction resistance ( $R_f$ ). The quasi-straight line represents the Warburg impedance ( $Z_w$ ), which is related to the solid-state diffusion of  $Li^+$  in the electrode materials [41,42]. The equivalent circuit at the open circuit voltage is used for data fitting. It is obvious that the impedance ( $R_f$ ) of electrodes decreases with the increase of the amount of  $x$ . It seems that the integration of  $Li_2MnO_3$  would increase the impedance of the electrode. Such phenomenon can be explained by the poor conductivity of  $Li_2MnO_3$  regions. [20,41] The higher surface charge-transfer resistance of the composite electrode is the reason why the rate capability of  $xLi_2MnO_3 \cdot (1-x)LiMn_{1.5}Ni_{0.5}O_4$  become worse with more  $Li_2MnO_3$  integrated. Among various compositions, when  $x \leq 0.3$ ,  $Li_2MnO_3$  has relatively little performance impact. Therefore,  $0.3Li_2MnO_3 \cdot 0.7LiMn_{1.5}Ni_{0.5}O_4$  is still very promising. To further improve its rate capability are under consideration, such as by morphology modification according to previous reports [34,43,44].

#### 4. Conclusions

A series of  $xLi_2MnO_3 \cdot (1-x)LiMn_{1.5}Ni_{0.5}O_4$  composites have been synthesized by co-precipitation method with layered  $Li_2MnO_3$  nanodomains well embedded in the  $LiMn_{1.5}Ni_{0.5}O_4$  spinel matrix. It is proven that the layered  $Li_2MnO_3$  structural unit substitution can greatly improve the structural stability of spinel structure when

cycled between 2 and 4.8 V, leading to much increased reversible capacity. The electrochemical performance indicates that better cyclability can be achieved as more  $\text{Li}_2\text{MnO}_3$  component is integrated into the spinel. Among various compositions,  $0.3\text{Li}_2\text{MnO}_3 \cdot 0.7\text{LiMn}_{1.5}\text{Ni}_{0.5}\text{O}_4$ , particularly, shows the excellent cyclability as well as a large reversible capacity. Ex-situ XRD results confirm that the cubic spinel phase in the composite with intermediate composition is very stable during cycling, which could be main reason for the superior cycle stability. Therefore,  $0.3\text{Li}_2\text{MnO}_3 \cdot 0.7\text{LiMn}_{1.5}\text{Ni}_{0.5}\text{O}_4$  is very promising as high capacity cathode for application in high energy density lithium-ion batteries.

## Acknowledgements

This research is supported by National University of Singapore through R265-000-426-731. J. Lu would like to thank Dr. Hailong Wang from Ningxia University, China for useful discussions.

## References

- [1] K. Kang, Y.S. Meng, J. Breger, C.P. Grey, G. Ceder, *Science* 311 (2006) 977–980.
- [2] B. Xu, D. Qian, Z. Wang, Y.S. Meng, *Mater. Sci. Eng. R* 73 (2012) 51–65.
- [3] X.-P. Gao, H.-X. Yang, *Energy Environ. Sci.* 3 (2010) 174–189.
- [4] Q. Zhong, A. Bonakdarpour, M. Zhang, Y. Gao, J.R. Dahn, *J. Electrochem. Soc.* 144 (1997) 205–213.
- [5] R. Alcántara, M. Jaraba, P. Lavela, J.L. Tirado, *J. Electrochem. Soc.* 151 (2004) A53–A58.
- [6] S.H. Oh, S.H. Jeon, W.I. Cho, C.S. Kim, B.W. Cho, *J. Alloys Compd.* 452 (2008) 389–396.
- [7] G.Q. Liu, L. Wen, Y.M. Liu, *J. Solid State Electrochem.* 14 (2010) 2191–2202.
- [8] N. Zhang, T. Yang, Y. Lang, K. Sun, *J. Alloys Compd.* 509 (2011) 3783–3786.
- [9] J. Xiao, X. Chen, P.V. Sushko, M.L. Sushko, L. Kovarik, J. Feng, Z. Deng, J. Zheng, G.L. Graff, Z. Nie, D. Choi, J. Liu, J.G. Zhang, M.S. Whittingham, *Adv. Mater.* 24 (2012) 2109–2116.
- [10] D. Liu, W. Zhu, J. Trottier, C. Gagnon, F. Barray, A. Guerfi, A. Mauger, H. Groult, C.M. Julien, J.B. Goodenough, K. Zaghib, *RSC Adv.* 4 (2014) 154–167.
- [11] K. Amine, H. Tukamoto, H. Yasuda, Y. Fujita, *J. Electrochem. Soc.* 143 (1996) 1607–1613.
- [12] R. Alcántara, M. Jaraba, P. Lavela, J.L. Tirado, *Chem. Mater.* 16 (2004) 1573–1579.
- [13] K. Ariyoshi, Y. Iwakoshi, N. Nakayama, T. Ohzuku, *J. Electrochem. Soc.* 151 (2004) A296–A303.
- [14] E.-S. Lee, K.-W. Nam, E. Hu, A. Manthiram, *Chem. Mater.* 24 (2012) 3610–3620.
- [15] M. Lin, S.H. Wang, Z.L. Gong, X.K. Huang, Y. Yang, *J. Electrochem. Soc.* 160 (2013) A3036–A3040.
- [16] B. Gee, C.R. Horne, E.J. Cairns, J.A. Reimer, *J. Phys. Chem. B* 102 (1998) 10142–10149.
- [17] M. Wagemaker, F.G.B. Ooms, E.M. Kelder, J. Schoonman, G.J. Kearley, F.M. Mulder, *J. Am. Chem. Soc.* 126 (2004) 13526–13533.
- [18] D. Pasero, N. Reeves, V. Pralong, A.R. West, *J. Electrochem. Soc.* 155 (2008) A282–A291.
- [19] S. Lee, Y. Oshima, E. Hosono, H. Zhou, K. Kim, H.M. Chang, R. Kanno, K. Takayanagi, *J. Phys. Chem. C* 117 (2013) 24236–24241.
- [20] M.M. Thackeray, S.-H. Kang, C.S. Johnson, J.T. Vaughey, R. Benedek, S.A. Hackney, *J. Mater. Chem.* 17 (2007) 3112–3125.
- [21] J. Li, Y. Xu, X. Li, Z. Zhang, *Appl. Surf. Sci.* 285 (2013) 235–240.
- [22] J. Liu, R. Wang, Y. Xia, *J. Electrochem. Soc.* 161 (2013) A160–A167.
- [23] O. Toprakci, H.A.K. Toprakci, Y. Li, L. Ji, L. Xue, H. Lee, S. Zhang, X. Zhang, *J. Power Sources* 241 (2013) 522–528.
- [24] C.S. Johnson, J.S. Kim, C. Lefief, N. Li, J.T. Vaughey, M.M. Thackeray, *Electrochem. Commun.* 6 (2004) 1085–1091.
- [25] S. Ivanova, E. Zhecheva, R. Stoyanova, D. Nihtianova, S. Wegner, P. Tzvetkova, S. Simova, *J. Phys. Chem. C* 115 (2011) 25170–25182.
- [26] C.S. Johnson, N. Li, J.T. Vaughey, S.A. Hackney, M.M. Thackeray, *Electrochem. Commun.* 7 (2005) 528–536.
- [27] A.D. Robertson, P.G. Bruce, *Chem. Mater.* 15 (2003) 1984–1992.
- [28] D.Y.W. Yu, K. Yanagida, Y. Kato, H. Nakamura, *J. Electrochem. Soc.* 156 (2009) A417–A424.
- [29] R.J. Gummow, A.D. Kock, M.M. Thackeray, *Solid State Ionics* 69 (1994) 59–67.
- [30] A.D. Robertson, S.H. Lu, W.F. Howard, *J. Electrochem. Soc.* 144 (1997) 3505–3512.
- [31] H. Huang, C.A. Vincent, P.G. Bruce, *J. Electrochem. Soc.* 146 (1999) 3649–3654.
- [32] Y. Shin, A. Manthiram, *Chem. Mater.* 15 (2003) 2954–2961.
- [33] M. Gu, I. Belharouak, J. Zheng, H. Wu, J. Xiao, A. Genc, K. Amine, S. Thevuthasan, D.R. Baer, J.G. Zhang, N.D. Browning, J. Liu, C. Wang, *ACS Nano* 7 (2012) 760–767.
- [34] L. Zhang, B. Wu, N. Li, D. Mu, C. Zhang, F. Wu, *J. Power Sources* 240 (2013) 644–652.
- [35] H. Wang, Y. Jang, Y.M. Chiang, *Electrochem. Solid-State Lett.* 2 (1999) 490–493.
- [36] A.R. Armstrong, A.J. Paterson, A.D. Robertson, P.G. Bruce, *Chem. Mater.* 14 (2002) 710–719.
- [37] P.G. Bruce, B. Scrosati, J.M. Tarascon, *Angew. Chem. Int. Ed.* 47 (2008) 2930–2946.
- [38] S. Kang, J.B. Goodenough, L.K. Rabenberg, *Chem. Mater.* 13 (2001) 1758–1764.
- [39] J.R. Croy, D. Kim, M. Balasubramanian, K. Gallagher, S.-H. Kang, M.M. Thackeray, *J. Electrochem. Soc.* 159 (2012) A781–A790.
- [40] K. Karthikeyan, S. Amareesh, G.W. Lee, V. Aravindan, H. Kim, K.S. Kang, W.S. Kim, Y.S. Lee, *Electrochim. Acta* 68 (2012) 246–253.
- [41] S.J. Shi, J.P. Tu, Y.Y. Tang, Y.X. Yu, Y.Q. Zhang, X.L. Wang, *J. Power Sources* 221 (2013) 300–307.
- [42] T. Zhao, S. Chen, L. Li, X. Zhang, R. Chen, I. Belharouak, F. Wu, K. Amine, *J. Power Sources* 228 (2013) 206–213.
- [43] S.J. Shi, Z.R. Lou, T.F. Xia, X.L. Wang, C.D. Gu, J.P. Tu, *J. Power Sources* 257 (2014) 198–204.
- [44] S.J. Shi, J.P. Tu, Y.D. Zhang, Y.J. Zhang, C.D. Gu, X.L. Wang, *Electrochim. Acta* 109 (2013) 828–834.